Fibre Optic-Based Patch Sensor for Crack Monitoring in Concrete Structures

Yago de Souza Gomes, Mohamed Saidi, Anna Lushnikova, Olivier Plé

Fibre Optic-Based Patch Sensor for Crack Monitoring in Concrete Structures

Yago de Souza Gomes, Université Savoie Mont Blanc, LOCIE, CNRS UMR 5271, INES, Le Bourget du Lac, France, yago.de-souza-gomes@univ-smb.fr
Mohamed Saidi, Université Savoie Mont Blanc, LOCIE, CNRS UMR 5271, INES, Le Bourget du Lac, France, mohamed.saidi@univ-smb.fr
Anna Lushnikova, Université Savoie Mont Blanc, LOCIE, CNRS UMR 5271, INES, Le Bourget du Lac, France, anna.lushnikova@univ-smb.fr
Olivier Plé, Université Savoie Mont Blanc, LOCIE, CNRS UMR 5271, INES, Le Bourget du Lac, France, olivier.ple@univ-smb.fr

---

Abstract: In the context of the necessity to monitor civil engineering structures for accident prevention, this paper presents the performance of an innovative optical fibre patch sensor that can be embedded or glued on the concrete's surface. The sensor is composed of a fabric comprising an optical fibre network. When employed in concrete structures, it is capable of detecting opening cracks in the order of 0.01 mm, thereby satisfying the regulatory standards for limit states (Eurocode2). This sensor is capable of accurately tracking the evolution of crack, including cyclic changes, by sensing both the increase and decrease in crack width. The procedure outlined in this paper includes a preliminary investigation into the influence of fibre diameter and density within the patch, which has revealed that fibres of 750 µm in diameter exhibit optimal performance, as well as the attachment method to concrete surfaces. Subsequently, the process of calibration is detailed, followed by numerous laboratory tests that were conducted on reinforced concrete samples of varying sizes. Comparisons and validations of optical fibre patch sensor measurements were performed using Digital Image Correlation, resulting in a sensitivity of the sensors reaching 0.01 mm/K, and an accuracy ranging between 0.1% and 1%. The discussion within this paper considers the installation of this new sensor both externally and internally within real reinforced concrete structures.

Keywords*:* embedded sensors; structural health monitoring (SHM); optical fibre sensors; crack detection; sensing technologies.

Introduction

The monitoring of reinforced concrete structures is becoming an increasingly crucial aspect of structural engineering. A variety of techniques for structural health monitoring, including fibre optic, piezoelectric, electrochemical, wireless and self-sensing technologies, with the aim of enhancing the reliability and the safety of concrete infrastructures as well as extending their operating lifespan [1]. Although reinforced concrete structures offer numerous advantages, including strength and durability, they frequently encounter a range of events that accelerate deterioration. These include earthquakes, heavy rainfall, hurricanes, freezing and heating, erosion, abrasion, chemical attacks, changes in the use of the structure that results in unexpected loads, and other factors. These events can collectively reduce the service lifespan of concrete structures and can induce significant safety risks on the structure. The real-time assessment of structural performance, considering both the ultimate and serviceability limit states, facilitates the early detection of anomalies such as defects or damage. This information aids in decision-making process concerning the rehabilitation, reinforcement, and/or destruction/reconstruction of the structure. [2].

A concrete structure is considered durable if it is able to provide the desired service life in its environment without incurring excessive maintenance and repair costs due to degradation. When engineers specify concrete for a project, they must consider the potential for deterioration that could affect the concrete in the specific environment over its intended service life. It is essential that the specifications encompass both the generic requirements for the desired class of concrete and specific measures to mitigate or prevent the effects of deteriorative influences at the project site [3].

The aging and deterioration of concrete structures is frequently evidenced by the emergence of cracks. These cracks frequently characterise damage to concrete structures in addition to other structural materials [4]. They can have a considerable impact on the structural integrity of the affected structures. In addition to compromising the overall strength and load-bearing capacity of the structure, such cracks also heighten the vulnerability to moisture and chemical penetration, particularly in the case of steel bars. In order to assess the risk associated with cracks in concrete structures, a commonly used diagnostic criterion is the crack width threshold. This threshold serves as an indicator of the severity of the crack and aids in determining the appropriate course of action. The specific crack width threshold varies depending on the type of structure and its intended purpose. In certain instances, Eurocode 2 considers a crack width threshold of approximately 0.2 mm as acceptable. However, in scenarios such as liquid retaining structures, this recommended crack width limit can be as low

as 0.05 mm [5,6]. This indicates that cracks below this threshold are typically categorised as hairline cracks and are deemed to have minimal impact on the performance and durability of the structure. However, cracks exceeding this threshold have the potential to impair the proper functioning or durability of the structure or cause its appearance to be unacceptable, requiring a more detailed examination.

The term "Structural Health Monitoring" (SHM) was defined by Villalba S and Casas J (2013) [7] as a set of strategies for the continuous or regular measurement and analysis of key structural and environmental parameters under operating conditions, for warning of abnormal states or accidents at early stages. Historically, the assessment of civil engineering infrastructures relied on periodic visual inspections conducted by trained professionals and sometimes completed with measurements [8]. However, this method could result in diagnostic errors due to imprecise interpretations by engineers leading to direct or indirect conclusions about factors such as displacement, strain, humidity, temperature, and other technical data taken punctually and not continuously. Currently, there are different ways to determine the stress state of a concrete structure [9], and for detecting cracks on concrete surfaces or within concrete structures [10–12]. There is a growing tendency towards the adoption of more intelligent surveillance techniques, characterised by remote monitoring in real time and the generation of automatic reports and alert systems. Deformation sensors play a crucial role in this context [9].

Fibre Optic-based strain sensors have emerged as a highly promising solution, significantly advancing the field of structural health monitoring. Despite the existence of traditional and well-stablished deformation sensors, such as strain gauges, linear variable differential transducers (LVTD) or vibrating wire strain gauges, the fibre optic (FO) sensors offer several advantageous properties. These include their light weight, electromagnetic passiveness and flexible installation. Over the past few decades, these sensors have been increasingly employed in civil engineering structures, enabling measurements over extensive lengths, exclusively along the optical fibres' direction. Depending on the installation setup, they can also access a 2D strain field [13,14]. Furthermore, some FO-based technologies are capable of measuring displacements with unparalleled precision [15–17].

Among the technologies that are based on fibre optics, some can be highlighted. One such example is the Fabry-Pérot interferometer sensor, which is a discrete sensor in which the measurement principle relies on a cavity, also called the Fabry-Pérot cavity, that separates two segments of uniaxial optical fibres. The configuration of a single mirror on either side of the cavity enables the differentiation of the rays emanating from the initial mirror and the subsequent mirror, thus facilitating the calculation of the distance between the two mirrors. This

distance can be a function of different phenomena [18,19]; The fibre Bragg grating sensor is a spot sensor that can be multiplexed to transform into a quasi-distributed sensor. It has been employed as a very effective tool for the monitoring of structures' health. The operational principle is based on the reflection of a specific wavelength spectrum by a grating situated in the core of the fibre. This consists of invisible periodic refractive index alterations which will result in a shift of the wavelength when subjected to deformation [20–25]. Another notable technology is the distributed optical fibre sensor (DOFS), which predominantly employs Rayleigh, Brillouin or Raman backscattering for the detection of vibration, strain and temperature variations. One of the most effective technologies is optical time-domain reflectometry (OTDR), which functions by transmitting highly coherent probe pulses and collecting Rayleigh backscattered (RBS) light to detect dynamic perturbation along the sensing fibre. These sensors are capable of continuous monitoring along the entire length of the fibre, over distances of up to several kilometres [26–28].

While each technique has its own set of advantages, it is important to acknowledge the limitations associated with each. Some of these limitations include cost, vulnerability to signal attenuation, a complex calibration process, a limited strain measurement range, and a complex fabrication process [29]. It is for these reasons that this project can be considered a valid and promising solution in the field of innovative sensors.

This work presents a novel fibre optic-based sensor, which can be embedded in concrete or attached to its surface, and analysis its performance. The sensor is comprised of a textile where fibres are woven parallel to each other, intercalating fibres connected to a light source and fibres connected to a photosensitive dispositive that provides accurate Correlated Colour Temperature (CCT), expressed in Kelvin (K). The signal is then obtained by the rays which escaped from the emitting fibres and entered the receiving fibres due to intentional creation of surface irregularities. The detailed attributes of this optical patch sensor are outlined in French Patent No. 3067806, officially registered under No. 1755382 [30].

The embedded and on-surface patch sensors will be discussed in turn. The sensor is capable of detecting opening cracks as small as 0.01 mm, within the regulatory limits. The sensor is capable of tracking the progression of the crack, detecting both widening and narrowing. The capacity to sense crack closure is crucial, especially given recent advancements in crack repairing techniques.

Methods

Components description

Light detector

The SENTMI (SENsor Textile Monitoring Infrastructures) project utilises, in its first version, a white LED OSLON SSL 150 “GW CSHPM1” (

a) b)

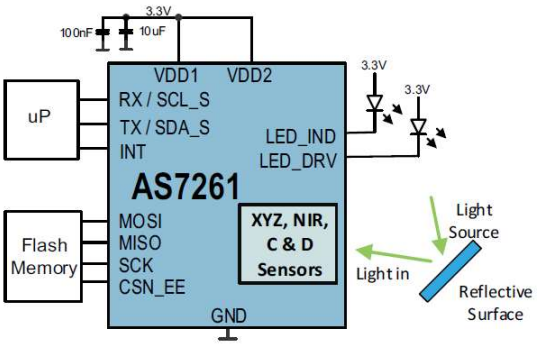

Fig 1-a) and the AS7261 sensor from ams OSRAM, which is a chromatic white colour sensor that provides XYZ colour coordinates consistent with the CIE (*"Commission Internationale de l'éclairage"*) colour space as well as the Near Infra-Red (NIR) spectrum (

b) b)

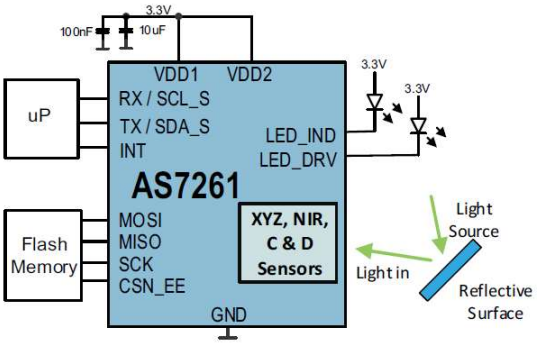

Fig 1-b). The spectral conversion is applied via two photodiode banks. Bank 1 converts data from the X, Y, Z and NIR photodiodes. Bank 2 processes data from the same X and Y photodiodes as well as the D (dark) and C (clear) photodiodes [31].

c) b)

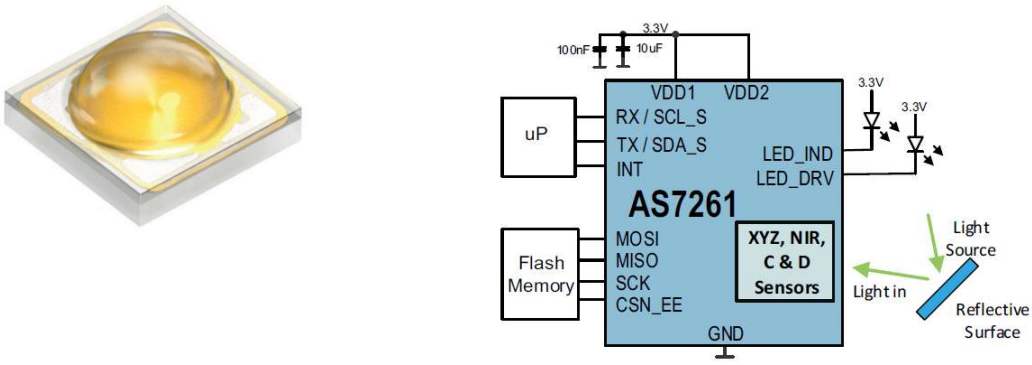

Fig 1. a) sensor's LED; b) AS7261 Chromatic White Color System

Textile sensor

An elastane fabric incorporates PMMA-based optical fibres that are woven in a parallel configuration. In the active zone (Fig 2), a technique of damage is employed to create intentional flaws on the surface of the FO cladding and on the interface between the FO core and cladding. This allows the passage of light to adjacent fibres. There are two groups of optical fibers. Emitting fibers are the ones connected to the white LED, while the receiving fibers are the ones connected to the AS7261. Those two groups of fibers are arranged in an intercalated configuration. The portion of the fibers that is not situated within the active zone is not subjected to the damaging technique. Consequently, in this portion of the fibers, the light travels in accordance with the principle of total internal reflection. This design ensures that the photodiodes exclusively detect fluctuations in the correlated colour temperature resulting from modifications in the active zone [30]. The diameter of the fibres and the density of fibres are significant factors influencing the sensitivity of the textile sensor. The density is defined as the number of fibres per centimetre in the direction denoted as "a" in Fig 2.

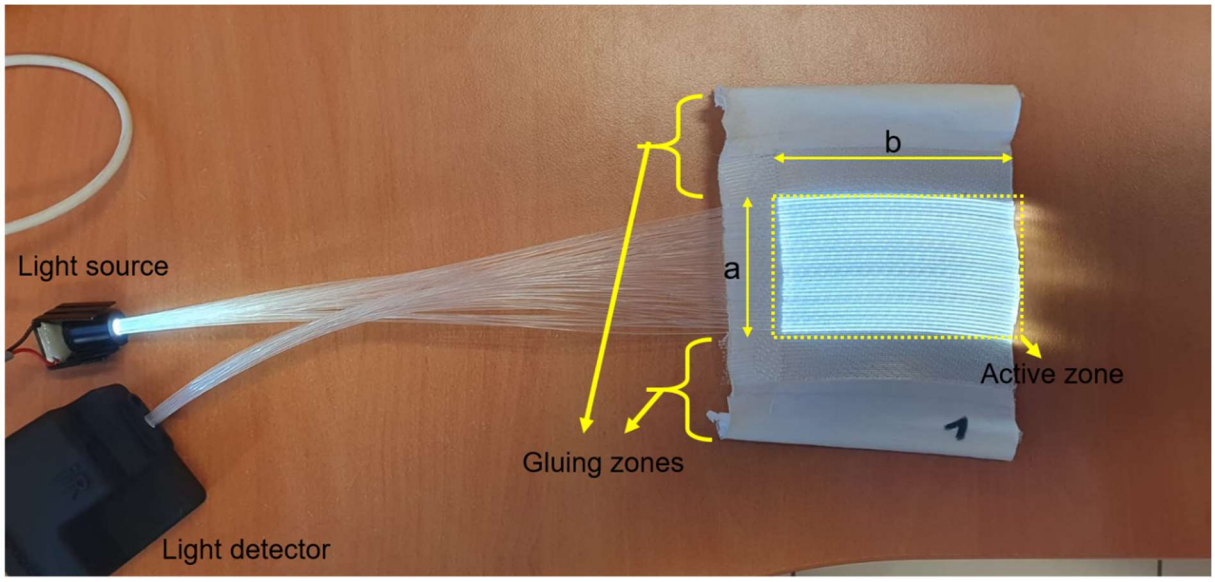

Fig 2. SENTMI fibre optic patch sensor

Parameters of sensor configuration

The optimal configuration for the optical patch sensors was determined by examining a range of parameters, including fibre diameter, fibre density, fabric size, and light power. Fiber diameters ranging from 250 to 750 µm (Fig 3-a) and densities between 7 and 26 optical fibres per cm were utilised for experimentation. Fabric of dimensions 30 × 30 mm², 50 × 50 mm², 50 × 150 mm², and 100 × 100 mm² were employed on different types of concrete samples (Table 1). The findings from assessing the patch's effectiveness in detecting and measuring deformation are presented in this paper.

a)

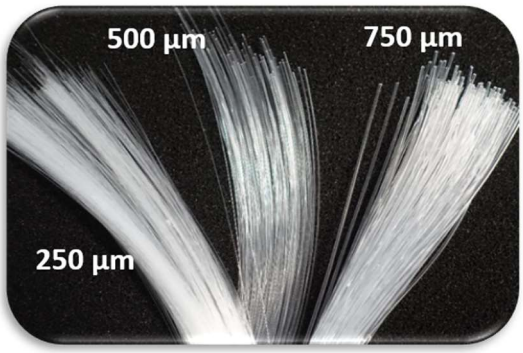

b)

c)

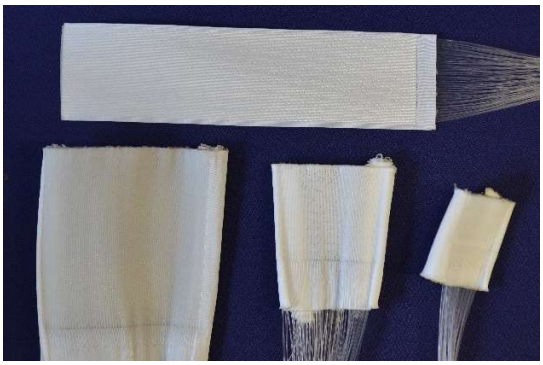

Fig 3. a) diameters used in the study; b) patch featuring 750 fibres connected to the LED; c) different patch sizes

Table 1. Configurations of patches preliminary studied

Dimensions a × b (mm²)	FO	Density (FO/cm)
100 × 100	250	7
		11.5
		18.5
		26 (max)
	500	7
		11.5
		18.5 (max)
	750	7
		11.5 (max)
50 × 150	500	7
		11.5
		18.5 (max)
50 × 50	750	11.5 (max)
	500	18.5 (max)
30 × 30	500	7
		11.5
		18.5 (max)

The objective was to enhance the sensor configuration, aiming to improve sensitivity. In this context, sensitivity is defined as the amount of displacement between the two edges of the sensor required to alter spectral coordinates by one unit or, equivalently, the amount of global strain needed to change spectral coordinates by one unit.

It was observed that an increase in the selected diameter resulted in a higher light spectrum coordinate and enhanced sensor sensitivity. Following initial observations, the 250 µm diameter was discarded due to its inferior performance in comparison to the other two diameters. A 650% increase in sensor sensitivity was observed between the 250 µm and 500 µm diameter ranges.

The number of fibres per cm also exerts an influence on the signal strength, with denser patches yielding stronger and more sensitive signals (Fig 4). For instance, a 750 µm diameter fiber presented a 16% enhancement in sensor sensitivity when the number of fibres per cm was increased from 7 to 11.5. However, it should be noted that there are limitations to the density of fibres of a given diameter. For example, fibres with a diameter of 750 µm are unable to reach the maximum density achievable with the other two types of fibre.

Considering these parameters, the initial configurations selected for further investigation were fibres with a diameter of 500 µm and a density of 18.5 fibres per cm and fibres with a diameter of 750 µm and a density of 11.5 fibres per cm, representing the maximum density for their respective diameters.

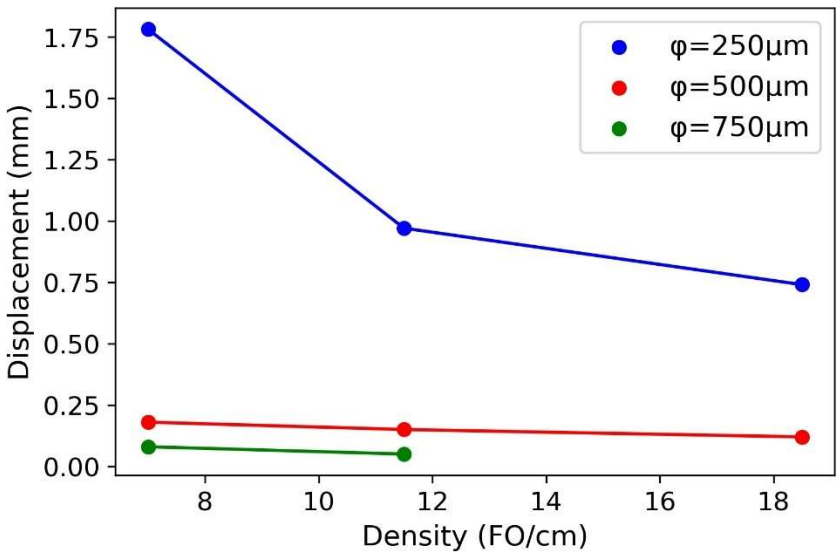

Fig 4. Comparison of the displacement needed for varying light signal, depending on the quantity of fibres per cm, for fibres in three different diameters.

The dimensions were selected on the basis of their suitability for use in the testing and calibration process. Given the dimensions of the specimens and the clamps employed in the calibration cycles, the 30 × 30 mm and 50 × 50 mm patches were deemed appropriate.

Patch calibration

In order to gain a deeper insight into the manner in which the patch responds to the displacement of its two edges, a calibration procedure was developed using digital image correlation as a means of comparison and validation. The calibration procedure is under the french patent number B256-B-69739 "Détecteur de déformation à base de fibres optiques, et procédé de calibration d'un tel détecteur" [32]. A series of patch configurations were subjected to uniaxial tensile tests, utilising a fabric tensile apparatus equipped with textile clamps. The procedure involved testing the patch individually by gripping its edges in a tensile machine (Step 1 from Fig 5), connecting the patch both to the light source and the detector (Step 2 from Fig 5) and subjecting it to cycles of stretching and releasing at a rate of 0.5 mm/min (Step 3 from Fig 5) to compute the equation of correlation (Step 4 from Fig 5). Prior to establishing a standard calibration procedure, the tests were conducted to verify the consistency of the patch's response when subjected to repeated stretching. The machine employs an electromechanical system, comprising a movable crossbar connected to the top clamp, which is guided in an up-and-down motion. At first, the movable crossbar (i.e., the clamp) was fixed at a distance from each other that allowed the textile sensor to remain flat but unstretched, thus representing a relaxed configuration. That was regarded as the initial position, defined as zero displacement. Subsequently, the crossbar was displaced by 2 mm in an upward direction, then by 2 mm in a downward direction (returning to the initial position) four times (blue plot in Fig 6-b). The sensor demonstrated excellent reproducibility, producing identical light signal outputs when decreasing CCT during stretching and recovering it upon returning to its initial tension state. This response appeared to follow a linear pattern, until a subsequent test involving a 3 mm displacement (red plot in Fig 6-b) revealed that the decrease CCT for a 3 mm stretch (20 K) was not directly proportional (150%) to the decrease observed during a 2 mm stretch (15 K). Therefore, the response is not strictly linear.

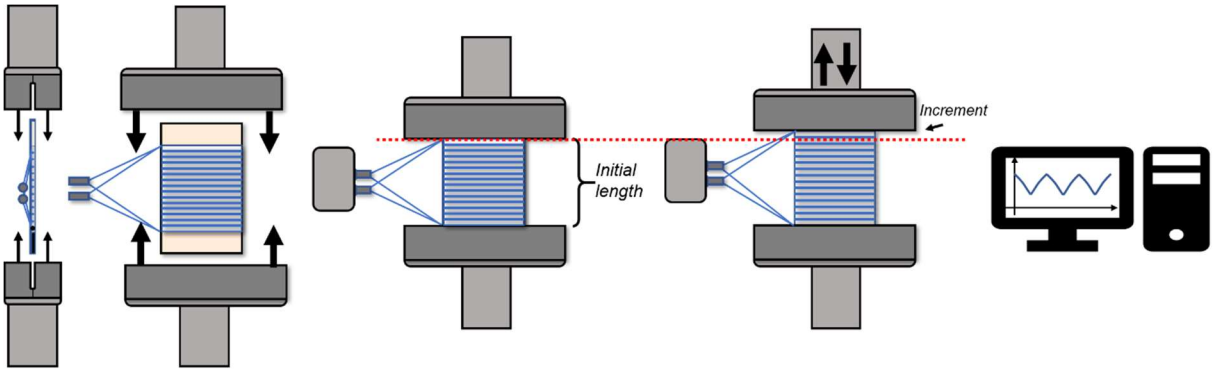

Fig 5. Steps for calibrating the SENTMI sensor for measuring cracks

a) b)

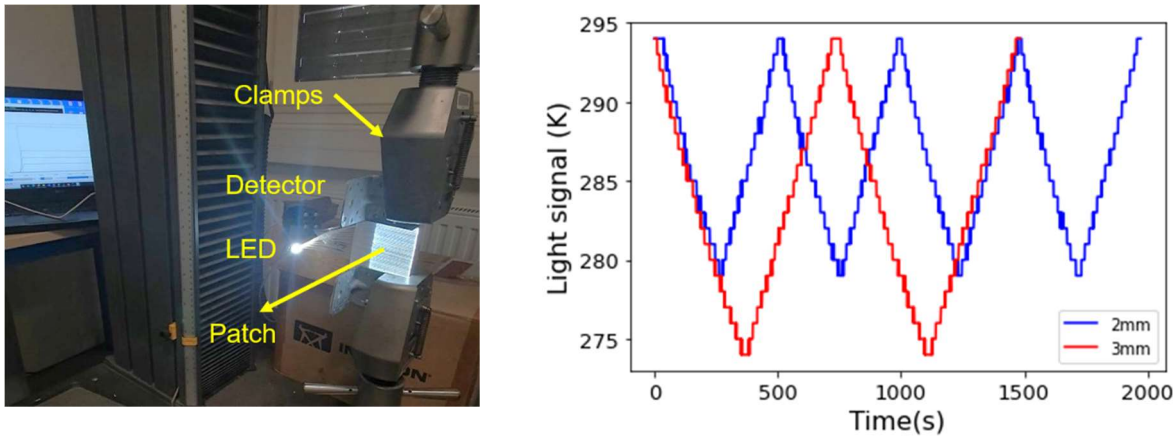

Fig 6. Calibration campaign of the SENTMI fibre optic textile sensor: a) SENTMI textile sensor being calibrated; b) Sensor's response to cycles of 2 mm and 3 mm extension and contraction

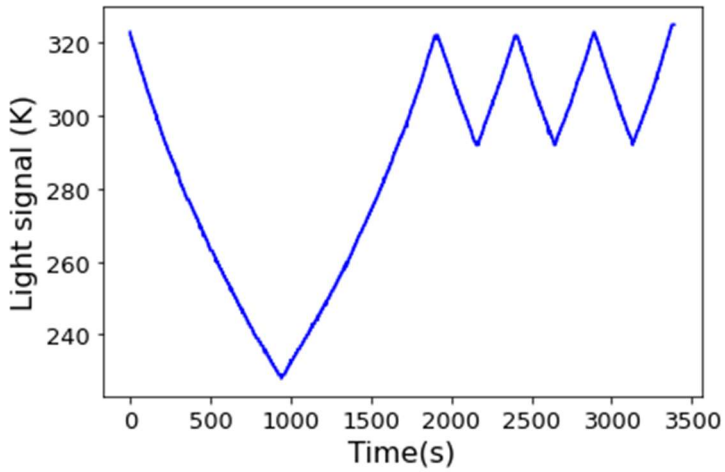

Fig 7. Full cycle of calibration

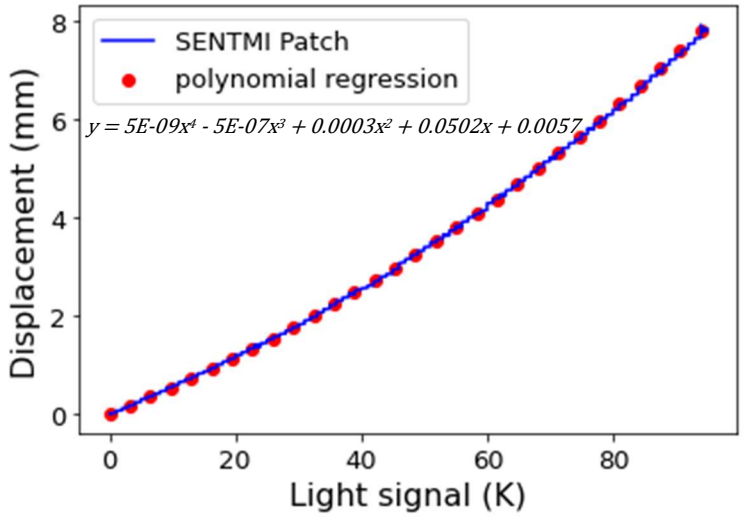

Fig 8. Equation of calibration through polynomial regression.

The adopted calibration procedure, which is to be applied to all the patches, consists in performing one extended stretch of 8 mm, during which the movable crossbar is displaced 8 mm upwards from its initial position. This is followed by a return to the initial position, a further 2 mm stretch, and a return to the initial position, three times (Fig 7). This procedure is undertaken in order to derive the correlation equation through polynomial regression (Fig 8) [32]. The post-treatment of the patch signal includes considering the initial value of light signal as the reference, indicating zero deformation, from which incremental changes can be calculated. The correlation coefficient, which scales the increment in light signal, represents the sensitivity of the sensor. For instance, a coefficient of 0.05 mm/K would be applied if each 0.05 mm of stretch corresponds to a variation of 1 unit in light spectrum coordinates. Therefore, this coefficient can be characterized as:

$$K = \frac{\partial d}{\partial l} \quad (1)$$

Where K is the coefficient of correlation, d is the displacement of one edge of the patch with respect to the other edge, and l is the correlated colour temperature.

Surface attachment method

The patches have been modified to include additional fabric borders surrounding the area where the glue is applied. In the initial stages of the project, the glue was applied directly to the surface of the patch's active zone (Fig 9-a). However, this method was modified due to concerns about potential reinforcement effects on the crack and sliding movements resulting from the interaction of the glue with the patch in the fracture zone.

Consequently, the adhesive is now applied to the non-active zone of the patch, which is distant from the crack. This region is not subjected to deformation, thereby ensuring that the two zones remain independent and are able to move with respect to each other.

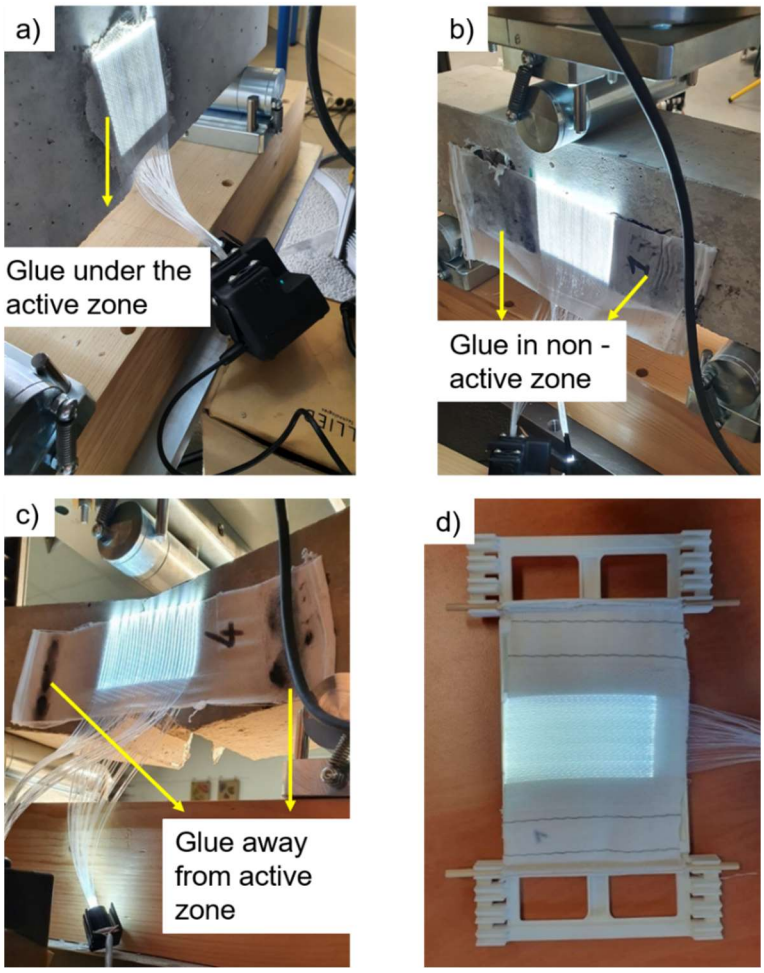

Fig 9. Methods of gluing the patch to the concrete's surface.

As the active zone reacts to the displacement between the two glued areas, it's not imperative for the adhesive zone to begin directly from the boundary of the active zone (Fig 9-b), referred to as method 1. Alternatively, the adhesive can be applied at a distance from the active zone, which is called method 2 (Fig 9-c). However, due to the highly deformable nature of the tissue material, the non-active zone between the fibres and the adhesive zones (in Fig 10) will absorb a portion of the overall deformation, resulting in an underestimation of the crack width.

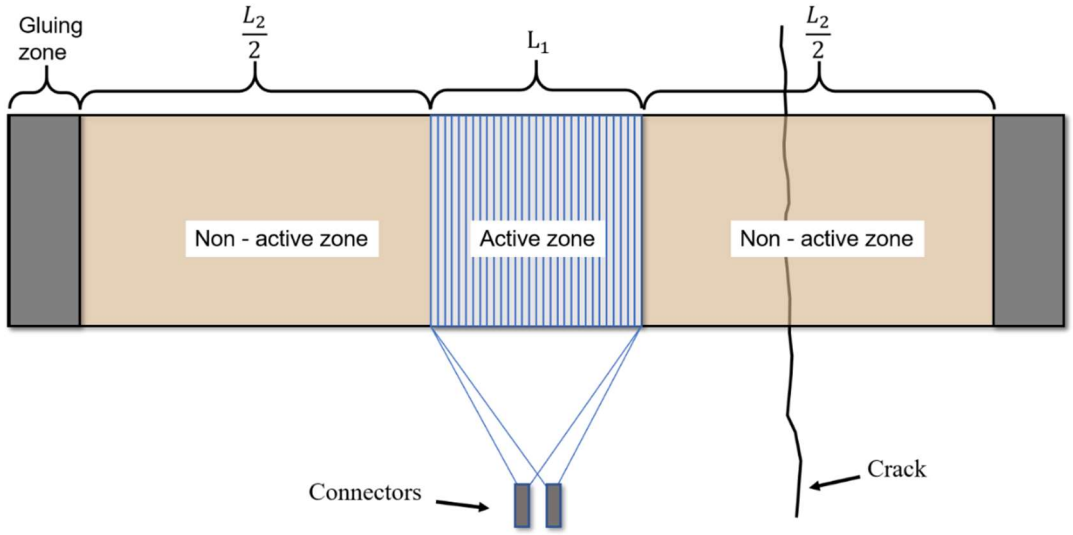

Fig 10. SENTMI sensor sketch of method 2.

For elastic materials, the ratio between the deformation ΔL and the initial length L_0 (L_1 + L_2) is expressed as strain ε as follow:

$$\varepsilon = \frac{\Delta L}{L_0} \tag{2}$$

When an object consists of two materials, a deformation applied to it will result in the deformation of both materials based on their respective moduli of elasticity. The overall deformation ΔL can be expressed in terms of strains and lengths as follows:

$$\Delta L = \varepsilon_1 \cdot L_1 + \varepsilon_2 \cdot L_2 \tag{3}$$

If the modulus of elasticity for and is equal, the increase in length in will be directly proportional to its length in relation to the total length between the two glued zones. This relationship can be presented as:

$$\Delta L_1 = \Delta L \cdot \frac{L_1}{L_1 + L_2} \tag{4}$$

297 This suggests that for a 1 mm crack, it represents 90% of the total length, the active zone
298 will experience a tensile strain of 0.1 mm. Consequently, the sensor exhibits a sensitivity that
299 is ten times lower. However, assuming the non-active zone is completely rigid (experiencing
300 zero strain), this would result in a total stretch of 1 mm in the active zone.
301 The patch illustrated in Fig 9-c was subjected to both gluing methods. The resulting
302 sensitivity was 0.05 mm/K for method 1 and 0.09 mm/K for Method 2. In Method 2, the glue
303 was applied at a distance of 2.5 cm from the edge of the active zone, which has a surface area
304 of 5 × 5 cm². Consequently, in this case, is equal to.
305 The Method 2 offers the advantage that, when the aim is to detect the onset of a crack, it
306 allows for an extension of the sensor's coverage length without requiring additional optical
307 fibres. Conversely, if the objective is to monitor an existing crack, method 1 is preferable.
308 The current gluing method employs an installation device, serving as a frame to ensure
309 standardized patch application (Fig 9-d). As the patch is flexible, manual application without
310 assistance can lead to varying levels of tension. The utilisation of the device ensures a consistent
311 pre-tension. This aspect is crucial, particularly when considering the transition from the
312 laboratory to the construction site. Consequently, the implementation method must be
313 straightforward and systematic in order to minimise the risk of errors.
314 ***Embedding method***
315 If the preceding technique is reserved for monitoring existing infrastructures, the patch can
316 also be incorporated into new reinforced concrete structures during construction. Initially, no
317 notches were made on concrete samples where SENTMI textile sensors were utilised (Fig 11-
318 a, Fig 11-b, and Fig 11-c). However, the absence of notches in the samples resulted in the
319 formation of significant crack openings, leading to excessively wide crack widths at the moment
320 of opening compared to the desired values in this study. Consequently, a method was employed
321 to insert the patch into the concrete specimens while still creating the necessary notch (Fig 11-
322 d). Concreting was done by first reaching the level of the bottom of the sensor, ensuring
323 standardized depth. The patch was then installed in conjunction with the prismatic wooden
324 piece that was divided into two parts, to accommodate the patch and secure it at a standard
325 distance from the lateral surface of the samples. The positioning was not centralised. The
326 patches were placed at a distance of 2 cm from one of the lateral surfaces in order to ensure
327 optimal positioning during testing in the flexural testing machine (Fig 12).

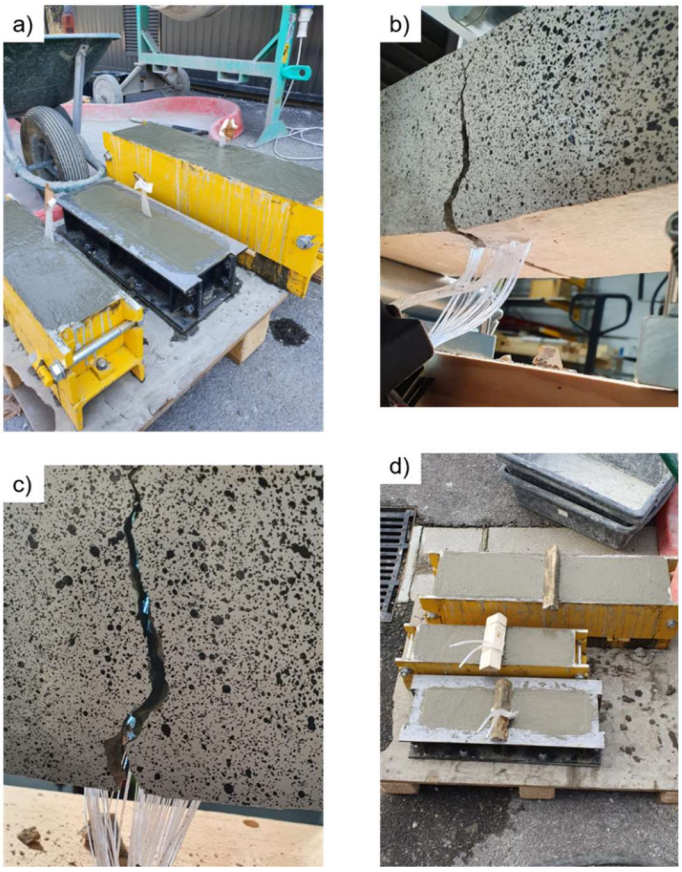

328

329 Fig 11. Concrete samples featuring embedded SENTMI textile sensors

330

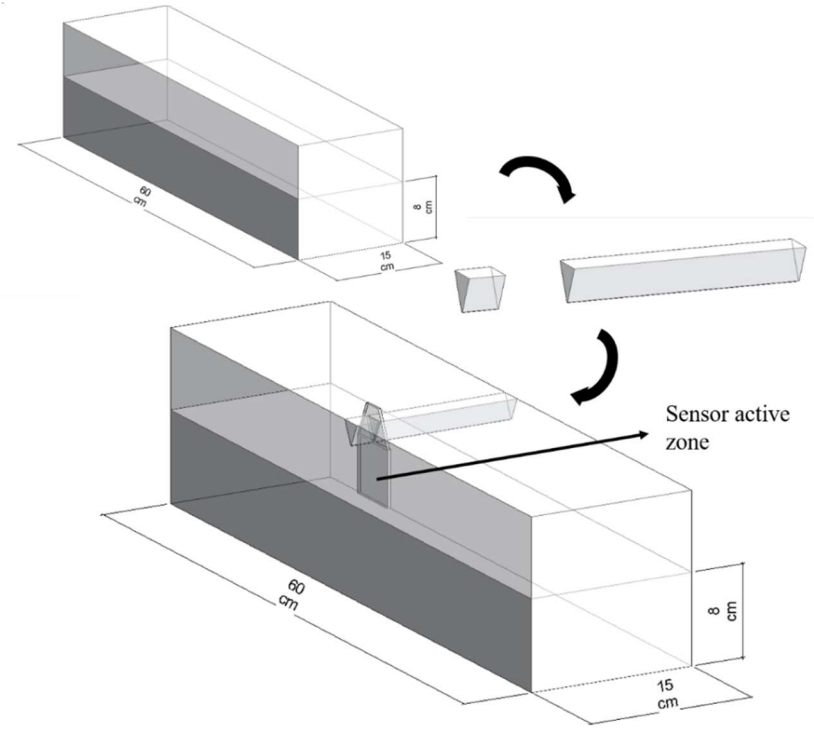

331

332 Fig 12. Method of embedding patch sensor in laboratory concrete samples

Remarks on the difference between on surface and embedded

An important difference between the operating principle of embedded patches and on-surface patches is that, when embedded, only cracks that occur in the active zone will be detected by the patch. The crack, as a discontinuity, occurring outside of the active zone will not result in the deformation of this zone. Moreover, this discontinuity results in the displacement of a limited number of fibres, one to the other, instead of a global strain throughout the active zone.

a) b)

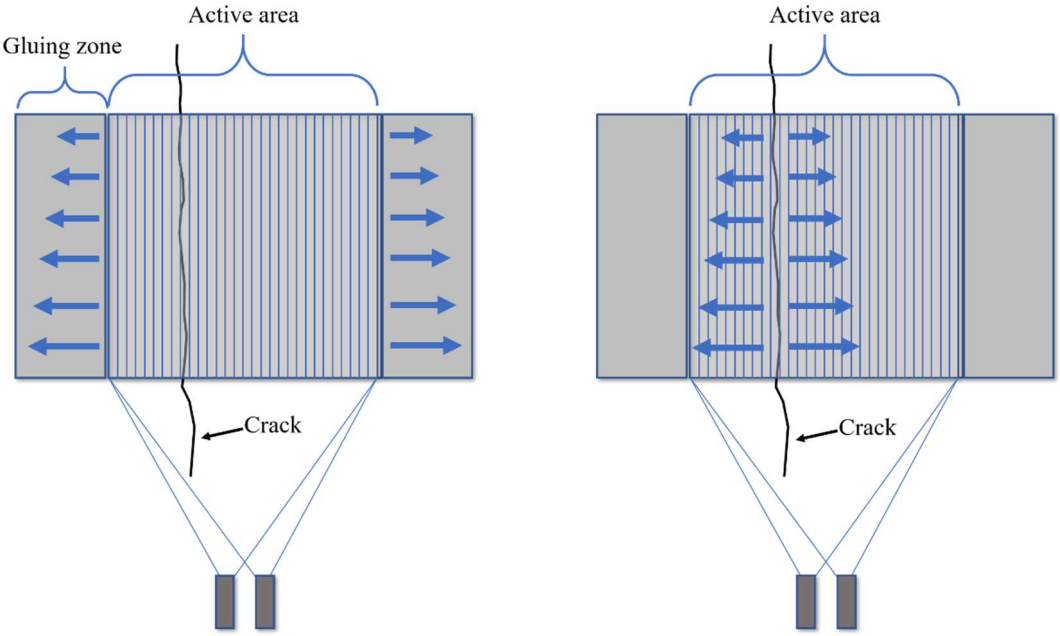

Fig 13. a) Sketch of on-surface patch crack behaviour; b) Sketch of embedded patch crack behaviour

In patches glued on the surface of the sample (Fig 13-a), the active zone is not bonded to the concrete. Consequently, any displacement between the two bonded zones results in a uniform displacement among the fibres. Conversely, in patches embedded within the concrete (Fig 13-b), the active zone adheres to the structure. Consequently, when a crack occurs, it induces localized deformation of the patch, resulting in localized displacement among a small number of fibres within the fracture zone.

Performance assessment method

A crack in a material is a discontinuity caused by the failure of atomic bonds to withstand forces [33]. In concrete, crack opening is a complex mechanical process influenced by material characteristics, loading conditions, and environmental factors. Cracks evolve from microcracks

into visible fissures. Initially, crack width is often microscopic and invisible to the naked eye, but it can expand as the load increases. The initial crack width varies based on factors such as the applied load, concrete's tensile strength, reinforcing elements, grain size, notches and defects, confinement arrangement, aspect ratio, and other geometric attributes [33,34].

The evaluation methodology encompasses several steps, including the fabrication of prismatic concrete samples of varying dimensions, the implementation of a calibration procedure, the attachment of the calibrated patch to the concrete sample, the mechanical testing of the sample to induce cracks, and an assessment of crack measurement accuracy through the use of Digital Image Correlation. This study utilised 40 samples measuring 10 cm × 10 cm × 40 cm, 8 samples measuring 15 cm × 15 cm × 60 cm (Fig 14-a), and 3 beams measuring 15 cm × 25 cm × 330 cm (Fig 14-b). For the sake of simplicity, these sample sizes will be referred to as sample types 1, 2, and 3 (corresponding to dimensions 10 × 10 × 40 cm^3, 15 × 15 × 60 cm^3, and 15 × 25 × 330 cm^3, respectively). A mixture of sand (0-6 mm), gravel (4-10 mm for sample type 1 and gravel 10 – 20 mm for the other two types), along with Vicat-Performat 52,5 N cement and water, was used. The concrete is designed to meet the specifications of C30/37 for severe exposure classes according to NF EN 1992-1-1 [5] regulations. To induce cracks in the region of interest, notches with a height of 2 cm were created in the sample for specimen types 1 and 2. This was achieved by placing a wooden triangular prism at the midpoint of the sample's length before pouring the concrete.

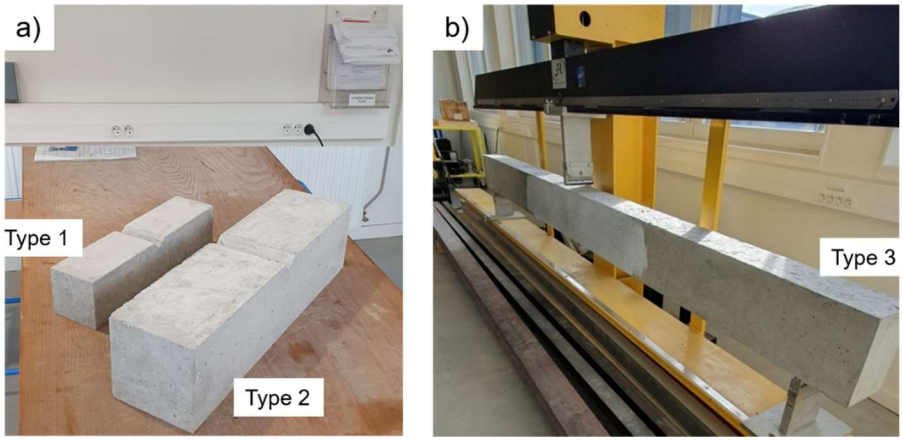

Fig 14. a) Sample sized 40 × 10 × 10 cm^3 and 60 × 15 × 15 cm^3; b) Beam of 330 × 25 × 15 cm^3 placed at the 3-point bending test machine

In this investigation, both Type 1 and Type 2 samples exhibited identical aspect ratios and notch sizes (**Erreur ! Source du renvoi introuvable.**). However, type 2 samples were

manufactured in two distinct configurations: with high-adhesion steel bars (reinforced) and without (non-reinforced). The reinforcement of type 2 specimens entailed the incorporation of two 8 mm diameter high-adhesion steel bars at the lower portion of the sample (Fig 15). Furthermore, three beams with no notches were reinforced (consisting of three 8 mm diameter high-adhesion steel bars at the lower section of the sample), with one of them additionally reinforced at the bottom surface with a layer of carbon-fibre-reinforced polymer (CFRP). CFRP, renowned for its exceptional properties, including lightweight, high strength, and resistance to high temperatures, holds significant promise for diverse applications across various fields, like structural repairs [35].

Table 2. Characteristics of specimens used in this study.

	Dimensions	Quantity	Reinforcement
Type 1	$10 \times 10 \times 40\ cm^3$	40	No
Type 2	$15 \times 15 \times 60\ cm^3$	5	No
Type 2	$15 \times 15 \times 60\ cm^3$	3	Bottom longitudinal reinforcement: $2 \times \emptyset 8\ mm\ CA - 50$
Type 3	$15 \times 25 \times 330\ cm^3$	2	Bottom longitudinal reinforcement: $3 \times\ \emptyset 8\ mm\ CA - 50$
Type 3	$15 \times 25 \times 330\ cm^3$	1	Bottom longitudinal reinforcement: $3 \times\ \emptyset 8\ mm\ CA - 50$ + CFRP layer reinforcement

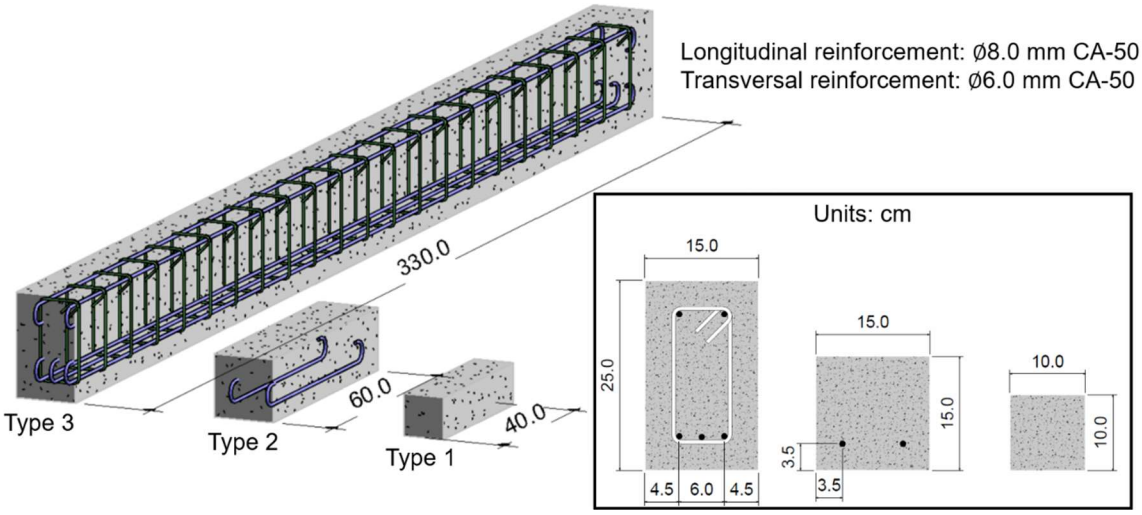

Fig 15. Sketch of the specimens used in this study.

Following calibration, the patches were attached to the surfaces of the specimens and subjected to a three-point bending test, a methodology similar to that employed by Gkantou M. et al. (2019) and Cimellaro G. P. et al. (2019) [36,37] in their investigation of crack detection in reinforced concrete structures. Specimens of types 1 and 2 were positioned symmetrically between two parallel supports and subjected to bending using a uniaxial displacement-controlled testing machine. The loading rate was 0.5 mm/min, and it was applied specifically to the central region of the sample adjacent to the upright section of the notch. In contrast, beams (type 3) underwent a stress-controlled three-point bending test at a rate of 0.05 kN/s. These modes dictate how the test is conducted and how data is gathered. In a displacement-controlled test, the testing machine applies a constant displacement rate to the specimen by moving the loading point at a predetermined speed. The resulting data is a function of the applied displacement and the force exerted. In a stress-controlled test, the testing machine responsible for maintaining a specific force level or load on the specimen. One disadvantage of a displacement-controlled test is that the device controls the opening crack, which may not accurately reflect real-world conditions. In a force-controlled test, the behaviour of the specimen subsequent to the peak load is determined by the applied force, which is a more realistic representation of the conditions that would be encountered in a real-world scenario.

A 2D Digital Image Correlation (DIC) technique was applied to validate the performed calibration (Fig 16), utilising a NIKON D7000 camera with a 60 mm focal length. In mechanical testing, DIC can be applied through few different methods [38,39]. It is a non-destructive optical technique [40–42] that relies on a series of high-resolution images captured during deformation, at a specified frame rate. The process commences by applying a random

speckle pattern on the specimen's surface, which serves as unique identification marker. As the material undergoes deformation, the camera captures images of the speckle pattern at various stages. The spatial shifts of pixels between the initial and deformed states are tracked by correlating their array of neighbouring pixels [43]. This technique allows for the computation of full-field displacement and strain maps, revealing localized deformations and strain distributions with high spatial resolution. DIC measurements can detect changes as small as a single pixel or even sub-pixel, in the order of 0.01 to 0.1 pixels. In ideal conditions, the accuracy of DIC displacement measurements can be in the range of 1 to 5 micrometres, or 0.01% of the field of view. Nevertheless, the precise physical length represented by this measurement will vary depending on factors such as the resolution of the camera and its distance from the surface being measured. Following the guidelines provided in the DIC Good Practices Guide by the International Digital Image Correlation Society (2017) [44], this study adopted a 2D-DIC approach. It is assumed that the sample maintains planar characteristics and a consistent stand-off distance throughout the testing process. To generate an appropriate speckle pattern for analysis, a white background colour was uniformly applied to the region of interest (ROI). Subsequently, black circular speckles were randomly superimposed on the white background in order to guarantee adequate contrast.

It is essential to ensure that the frame rate employed aligns with the anticipated rate of variation of the quantity of interest (QOI) in order to guarantee accurate results. If the displacement between frames is excessive, the DIC algorithms may encounter difficulties in locating the subset position within the resulting images [44]. In this study, a frame rate of 0.2 fps and a exposure time of 1/500 seconds were selected. The captured images have a resolution of 300 dpi and a size of 4928 × 3264 pixels. The images were subsequently processed using GOM Correlate 2018 software [45].

In this scenario, the Region Of Interest (ROI) corresponds to the surface area adjacent to the crack, and the height of the ROI is the height of the textile sensor. This height limitation dictates the extent to which the fiber optic textile can sense and respond to deformation. The dispositive will sense the overall deformation, which is the incremental distance from the left edge to the right edge of the textile. In bending tests, such as the three-point bending test, the crack width varies; it is wider at the bottom and narrower at the top, forming a triangular shape (Fig 16-a). The patch yields a single measurement representing the average crack width, as the variation in crack width relative to height is nearly linear. Consequently, the patch provides the crack width value for the mid-height.

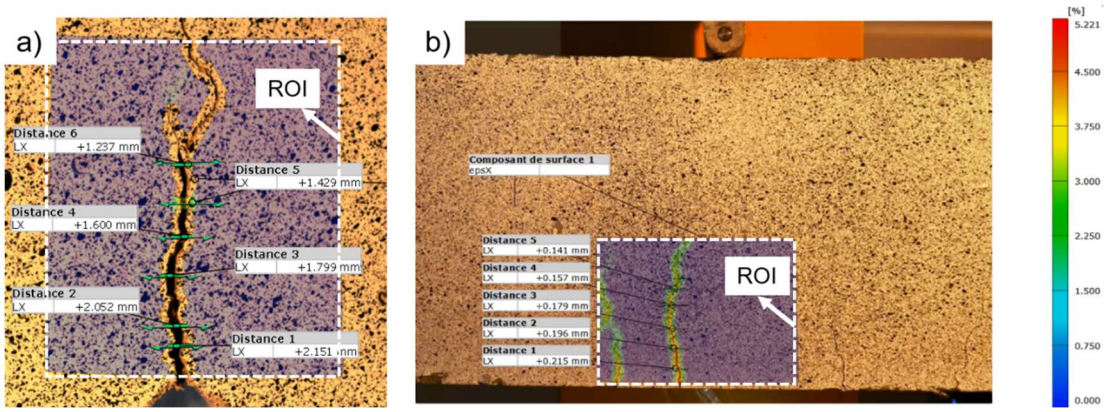

Fig 16. 2D Digital Image Correlation (DIC) performed at GOM Correlate 2018 Software: a) sample size 10 × 10 × 40 cm^3; b) Reinforced beam.

Python modelling environment was utilised to transform the export files from the sensor and from DIC analysis into a graphical comparison. This post processing includes reading both csv files (from sensor and from DIC exports), fixing the initial absolute value of light signal as zero, applying the equation of calibration on the values of increment in light signal in order to obtain an output in millimetres, and plotting both lines in a single graphic.

Results

Crack detection

The diverse characteristics of the samples result in distinct patterns of crack initiation and propagation. One notable distinction lies in the width of the crack upon its initial opening. This disparity in crack width is not only attributed to differences in sample characteristics but also to the inherent heterogeneity of concrete as a material. It is of great importance in order to examine such variations in crack width at the onset of opening, particularly given the crucial role of the sensor in detecting sudden crack openings or rapid crack developments, in addition to gradual and smooth crack propagation.

It is observed that these sudden crack openings are observed predominantly present in specimens lacking reinforcement, which constitute the majority of samples utilised in this study. Fig 17- illustrates the results of a three-point bending test conducted on a Type 1 sample. The image on the left depicts the final photograph taken prior to the emergence of the crack, while the image on the right captures the subsequent moment. In contrast, Fig 17-a, depicts a type 3 sample, a steel-reinforced concrete beam (unreinforced by CFRP). In this instance, the crack progresses from a microscopic to a macroscopic manifestation. The image on the left depicts the moment preceding the appearance of the crack, while the image on the right illustrates the subsequent moment. In both scenarios (Fig 17), the photos are captured at a 5-second interval,

consistent with the selected frame rate. Measurements conducted via digital image correlation reveal that the type 3 sample in Fig 17-a exhibited an initial crack width of 3.5 µm, whereas the type 1 sample in Fig 17-b displayed an initial crack width of 1.078 mm. As previously stated, the heterogeneous nature of concrete results in varying crack opening values even among specimens of the same type, as the results in the coming section will demonstrate.

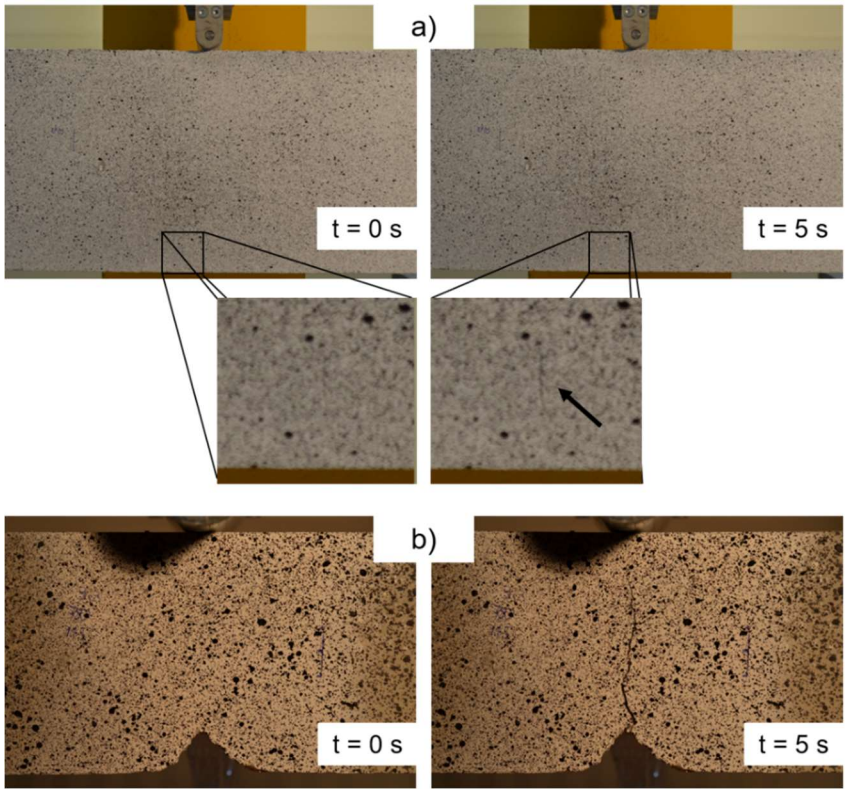

Fig 17. Crack opening onset a) Sample type 3; b) Sample type 1.

In consideration of the sensor's demonstrated sensitivity, when installed on the beam, the patch is capable of detecting a gradual increase in crack width from the onset. With a sensitivity of 0.004 mm/K for the patch affixed to the beam and a force rate of 0.05 kN/s, an average increment of 1 unit of light spectral coordinates occurs approximately every 14 seconds (Fig 18-a). Conversely, for specimen type 1, the patch registers crack opening as an almost instantaneous displacement of approximately 1 mm. In this instance, a sensitivity of 0.07 mm/K is obtained for the patch in use, resulting in an increment of 15 units of CCT within 1.09 seconds, which represents the sensor's acquisition time (Fig 18-b).

a) b)

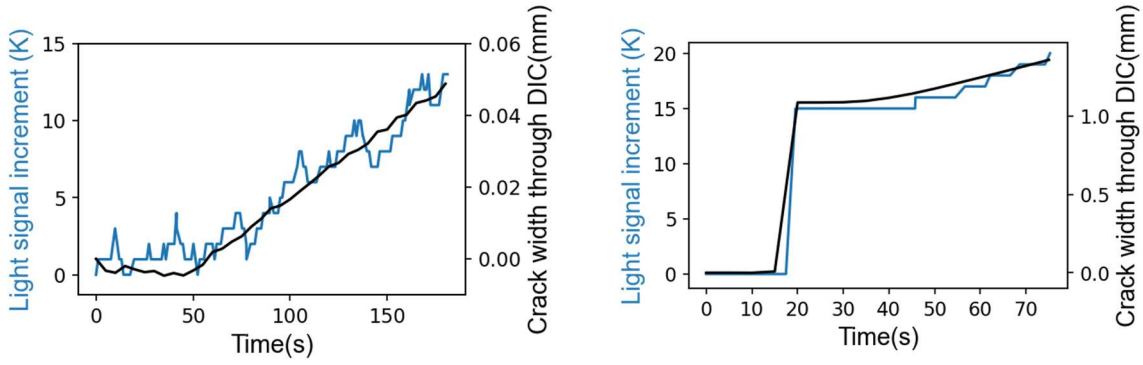

Fig 18. Crack detection a) Type 3; b) Type 1.

Crack width evolution track

The light signal measurements collected over time by the patch, along with the crack width measurements at mid-height of the patch position, obtained via Digital Image Correlation, underwent processing using Python, allowing for the application of correlation equations. Enhancements in patch configurations have significantly improved the sensor's sensitivity. Through refinement of these configurations, a sensor sensitivity of 0.004 mm/K and an accuracy of 0.1% to 1% has been achieved, as shown in Fig 19. This figure presents 14 graphs, where each of them corresponds to the result one flexural test in a specimen, comparing the sensor measurement (blue line) of crack width to the Digital Image Correlation corresponding measurement of crack width (red line). Measurements were conducted on samples of different types and sizes, as indicated in each image. Here, sensor sensitivity denotes the minimum increase in crack width (in mm) necessary to result in one unit change in CCT.

Upon examination of the lines, it becomes evident that the patch signal closely mirrors the onset and advancement of the crack. The lines exhibit a high degree of alignment. Initially, the crack width line experiences a rapid surge as the crack initiates in specimens of types 1 and 2, followed by a more gradual and consistent progression. Periodic abrupt increases occur sometimes (Fig 19-a) Fig 19. SENTMI sensor performance in following crack widthdue to material heterogeneity, such as aggregate rupture, introducing non-linearities.

The patch efficiently tracks both the gradual evolution and sudden spikes in crack width, demonstrating its capability to accurately capture these fluctuations and providing valuable insights into crack behaviour.

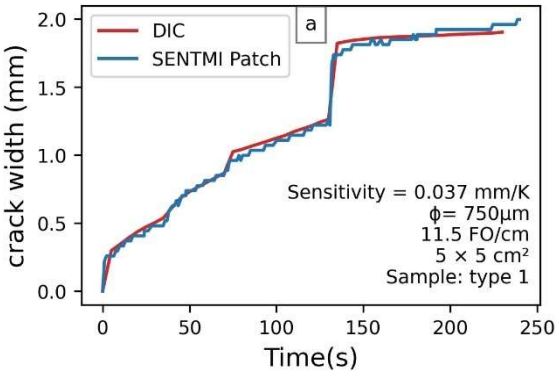
a
DIC
SENTMI Patch
crack width (mm)
Time(s)
Sensitivity = 0.037 mm/K
ϕ= 750μm
11.5 FO/cm
5 × 5 cm²
Sample: type 1

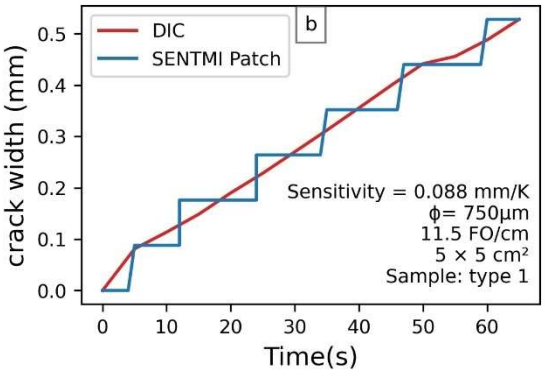
b
DIC
SENTMI Patch
crack width (mm)
Time(s)
Sensitivity = 0.088 mm/K
ϕ= 750μm
11.5 FO/cm
5 × 5 cm²
Sample: type 1

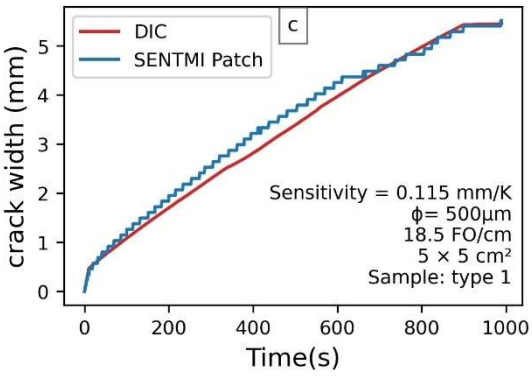
c
DIC
SENTMI Patch
crack width (mm)
Time(s)
Sensitivity = 0.115 mm/K
ϕ= 500μm
18.5 FO/cm
5 × 5 cm²
Sample: type 1

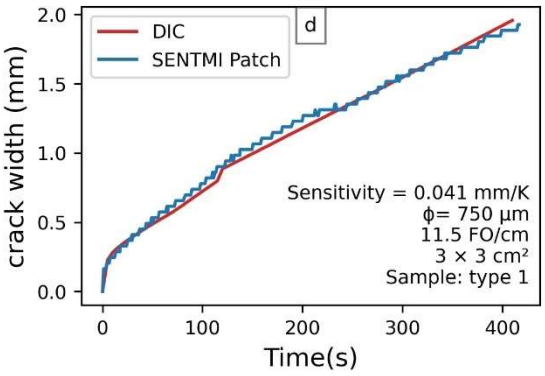
d
DIC
SENTMI Patch
crack width (mm)
Time(s)
Sensitivity = 0.041 mm/K
ϕ= 750 μm
11.5 FO/cm
3 × 3 cm²
Sample: type 1

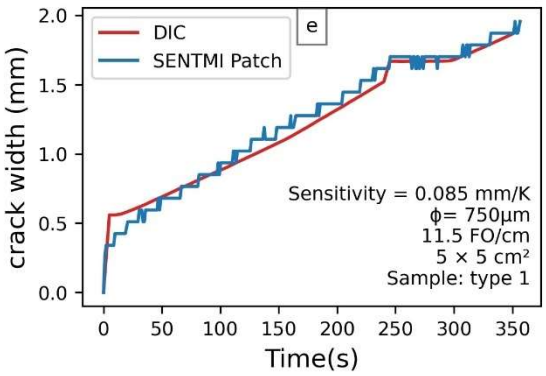
e
DIC
SENTMI Patch
crack width (mm)
Time(s)
Sensitivity = 0.085 mm/K
ϕ= 750μm
11.5 FO/cm
5 × 5 cm²
Sample: type 1

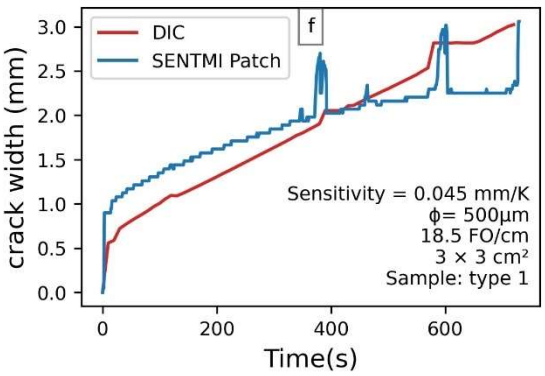
f
DIC
SENTMI Patch
crack width (mm)
Time(s)
Sensitivity = 0.045 mm/K
ϕ= 500μm
18.5 FO/cm
3 × 3 cm²
Sample: type 1

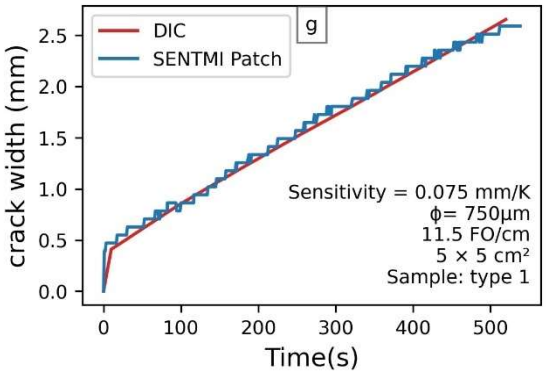
g
DIC
SENTMI Patch
crack width (mm)
Time(s)
Sensitivity = 0.075 mm/K
ϕ= 750μm
11.5 FO/cm
5 × 5 cm²
Sample: type 1

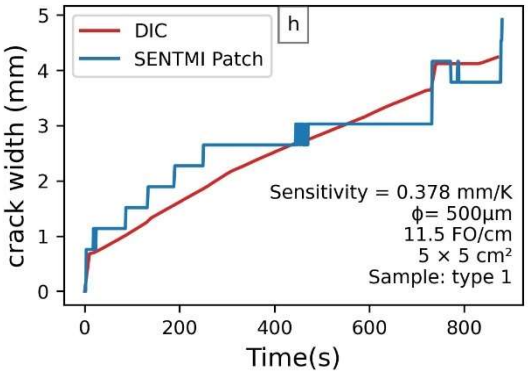
h
DIC
SENTMI Patch
crack width (mm)
Time(s)
Sensitivity = 0.378 mm/K
ϕ= 500μm
11.5 FO/cm
5 × 5 cm²
Sample: type 1

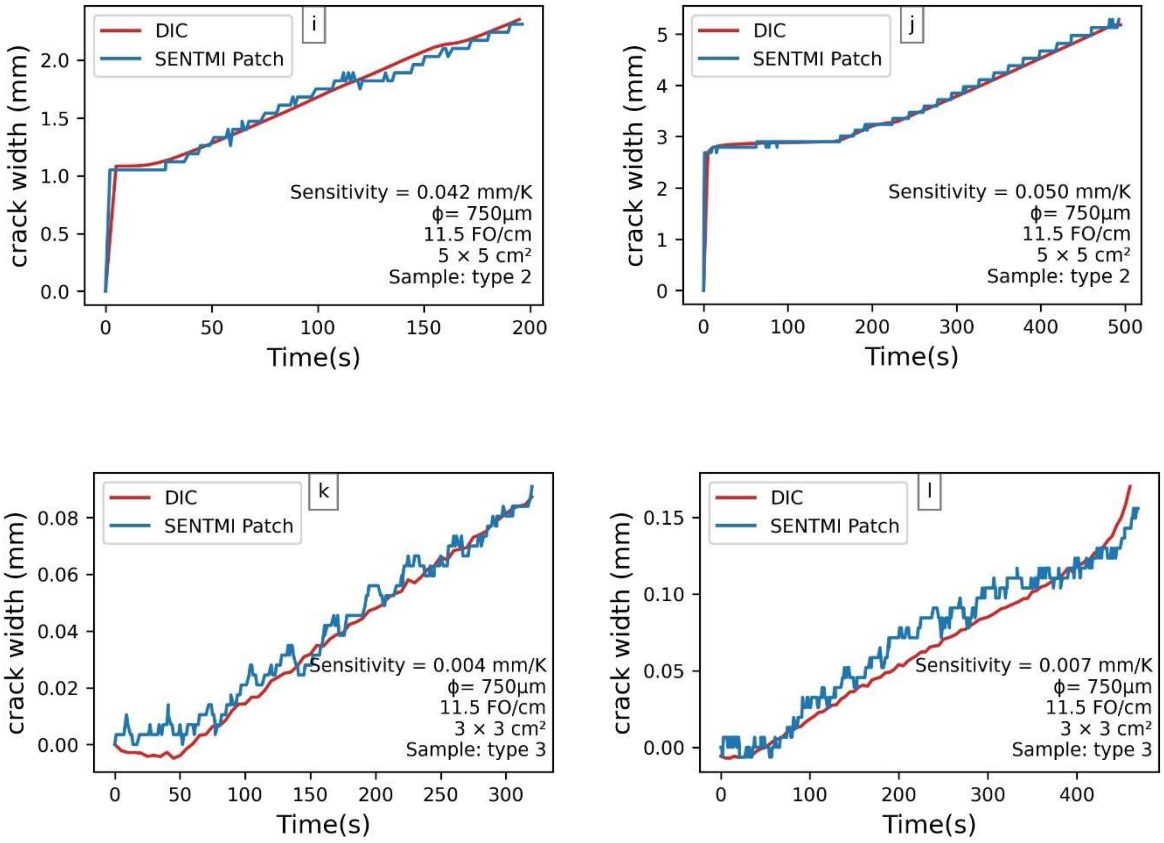

Fig 19. SENTMI sensor performance in following crack width

Cyclic test

It is crucial not only to monitor the evolution of crack openings, i.e., the increase in crack width, but also its converse, the decrease in crack width. The capacity of these sensors to measure displacements in both tension and compression modes is indispensable for a thorough understanding of structural integrity. In the field of civil engineering, where structures are subjected to a multitude of loads, including thermal gradients, wind, seismic forces, and traffic vibrations, deformation sensors ensure precise and reliable monitoring of structural responses. This bidirectional capability enables engineers to identify potential vulnerabilities, anticipate structural failures, and implement timely maintenance or corrective measures to comprehensively assess a material's mechanical properties.

Furthermore, measuring the variation of crack width in both directions assists engineers in monitoring the process of structural repair. Various methods exist to repair cracks in concrete, including the injection of fibres, epoxy resin, or the application of a carbon-fibre-reinforced layer [46].

For this test, a carbon-fiber-reinforced polymer (CFRP) layer was appropriately utilized to reinforce the bottom (tensile area) of the beam. Apart from its utility in repair applications, this beam has an advantage: due to the presence of the carbon layer, it could withstand higher loads

across numerous load and unload cycles, facilitating cyclic testing. The elastic properties of CFRP enable the cracks to nearly close during unloading. The high strength of this material enables it to deform elastically under stress and revert to its original shape upon stress removal, given the applied loads[47].

In order to evaluate the beam reinforced with a layer of CFRP, a force-controlled three-point bending test was conducted. Initially, a pre-charge of 3.2 KN was established. From this point, the load progressively increased to 10 KN, then returned to 3.2 KN, repeating this cycle three times. Subsequently, three additional cycles were performed, with the load reaching 18 KN before reverting to 3.2 KN. Finally, three additional cycles were conducted, elevating the load to 26 KN before returning to 3.2 KN. The results are presented in Fig 20.

The sensor exhibited reliable performance, accurately tracking the crack's progression during both opening and closing phases, although limited by the patch's sensitivity, set at 0.05 mm/K for this test. Therefore, when the force reached 18 KN, for instance, resulting in a crack width of 0.19 mm, the sensor would display either 0.15 mm or 0.2 mm.

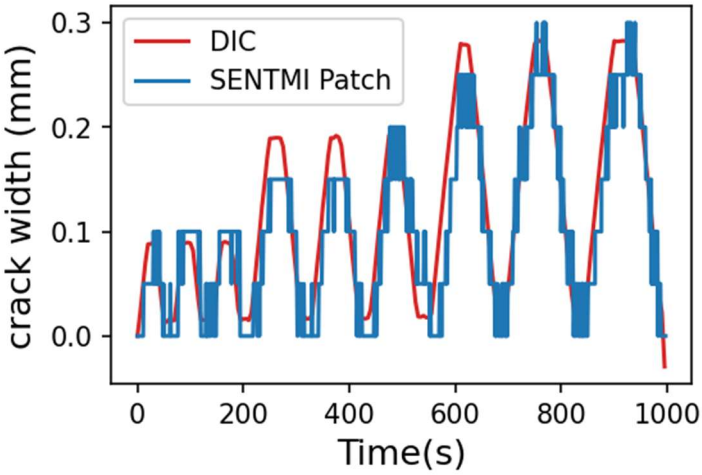

Fig 20. Sensor's performance in a cyclic test

Embedded patches

The capacity to function within the internal structure of concrete is a critical attribute for a displacement-measuring sensor. This is particularly significant in various construction scenarios such as bridges or dams, where the installation of the sensor during concrete pouring will be more practical, because re-accessing certain areas of the structures afterwards can be challenging. Additionally, the internal behaviour of the structure may differ from its surface behaviour, or cracks may arise first internally and propagate towards the exterior of the

structure. Consequently, internal fracture zones may be important for the professionals in charge to keep track of [48,49].

The embedded SENTMI patches demonstrated consistent performance comparable to their on-surface approach version, effectively monitoring the progression of cracks with a similar Mean Relative Error (MRE) that the best on-surface patches presented, ranging between 0.1% and 1%. Results are presented in Fig 21 on four samples tested under two different configurations for density and diameter of optic fibres.

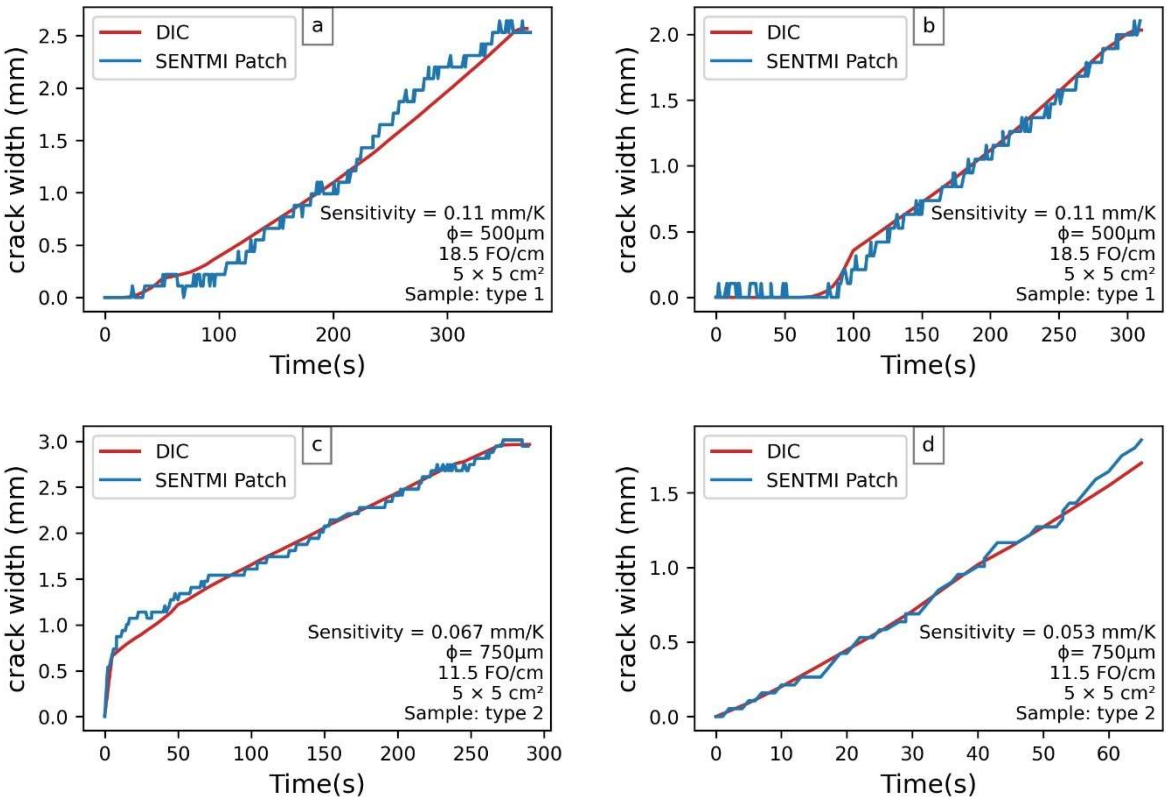

Fig 21. Results of crack width evolution for embedded patches

Conclusion

This work presents the initial key discoveries of a new fibre optic-based sensor developed for the purpose of structural health monitoring. The sensor patch, which can be embedded or affixed on a concrete structure surface, comprises a textile component containing two sets of optical fibres: one set linked to a light source (emitting fibres) and the other to a light sensor (receiving fibres). The deformation of the textile causes spectral coordinate variations, measured in correlated colour temperature, providing crucial data for structural assessment. Initially, the study concentrated on identifying configurations capable of achieving a sensitivity under the limits of recommended crack width limits, thus enabling the detection of minor

displacement. Sensitivity is defined as the amount of displacement between the two edges of the sensor required to result in the variation of the spectral coordinates by one unit. Therefore, the most sensitive sensors present a lower amount of displacement needed for measurement variation. The parameters under analysis included the diameter of the optical fibres, the density of optical fibres per centimetre, and the dimensions of the fabric.

It was observed that larger diameters and higher densities of optical fibres were associated with stronger light signals and enhanced sensor sensitivity. As a result, the optimal configuration was determined to be optical fibres with a diameter of 750 µm and a density of 11.5 fibres per cm. This density represents the maximum number of fibres of this diameter that can be accommodated within a width of 1 cm.

The installation methods for textile sensors on concrete surfaces were investigated. The distinction between methods 1 and 2 lies in the proximity between the adhesive zone and the sensitive region of the fabric. In method 1, the adhesive zone begins from the edge of the active region, causing the active zone to absorb all the deformation resulting from the discontinuity (crack) between the two adhesive zones. As a result, method 1 offers higher sensor sensitivity, up to 0.004 mm/K. Conversely, in method 2, the adhesive is applied at a distance from the active zone, reducing sensor sensitivity but expanding the measurement field, which is described as the gap between the two adhesive zones. A similar patch was tested using both methods and it attainted a sensitivity of 0.05 mm/K in method 1, while for method 2 it attainted a sensitivity of 0.09 mm/K. In method 2, the glue was applied 2.5 cm from the edge of the active zone, which is 5 × 5 cm^2. Patches were also embedded into the concrete specimens, using a prismatic piece of wood to create the notch and fix the position of the textile sensor.

Once the optimal sensor configuration and its installation system has been identified, calibration was carried out. A series of stretching and releasing cycles was conducted in order to compute the equation of correlation via polynomial regression. The calibration was followed by the application of the textiles to concrete specimens of varying dimensions. These samples underwent a three-point bending test to induce cracking, after which the performance of the sensors was evaluated using digital image correlation. The mean relative error for the embedded and glued patches across all sample types was found to be between 0.1% and 1%.

The diverse geometry and reinforcement of the specimens enabled the sensor to demonstrate its capacity to detect both gradual and abrupt crack initiations. The progression of the cracks, including both opening and closing phases, was analysed. The preliminary results are promising, with a sensitivity of up to 0.004 mm/K and a mean relative error for the embedded and glued patches across all sample types was found to be between 0.1% and 1%.

In the context of large structures, cracks may emerge as a consequence of mechanical and thermal stresses. It would be beneficial to investigate the impact of temperature on the optical patch sensor in both damaged and undamaged structures in the subsequent phase of this study.

Data availability

Some or all data of this study are available from the corresponding author upon reasonable request.

Acknowledgement

The realization of this project, known as SENTMI, has been made possible through financial support from La Région AURA (PSPC 2020) and BPI France. The success of this study owes much to the dedication and collaborative efforts of various entities, including Leon Grosse, Inouid, Brochier Technologies, and the LOCIE laboratory at the University of Savoie Mont Blanc. The authors extend their gratitude to Pellier Francois and Marie Allain from Léon Grosse company, Brochier Cedric and Richaud Martin from Brochier Technologies company, and Briand Didier from Inouid firm for their valuable insights and discussions.

References

[1] S. Taheri, A review on five key sensors for monitoring of concrete structures, Constr Build Mater 204 (2019) 492–509. https://doi.org/10.1016/j.conbuildmat.2019.01.172.

[2] W.H. Duan, Q. Wang, S.T. Quek, Applications of piezoelectric materials in structural health monitoring and repair: Selected research examples, Materials 3 (2010) 5169–5194. https://doi.org/10.3390/ma3125169.

[3] B. Mather, Concrete durability, Cem Concr Compos 26 (2004) 3–4. https://doi.org/10.1016/S0958-9465(02)00122-1.

[4] H. Al-Karawi, R.U.F. von Bock und Polach, M. Al-Emrani, Crack detection via strain measurements in fatigue testing, Strain 57 (2021). https://doi.org/10.1111/str.12384.

[5] CEN (European Committee for Standardization), EN 1992-1-1 (2004): Eurocode 2: Design of concrete structures - Part 1-1: General rules and rules for buildings, Brussels, Belgium: CEN., (2004).

[6] CEN (European Committee for Standardization), EN 1992-3 (2006): Eurocode 2: Design of concrete structures - Part 3: Liquid retaining and containment structures, 2006.

[7] S. Villalba, J.R. Casas, Application of optical fiber distributed sensing to health monitoring of concrete structures, Mech Syst Signal Process 39 (2013) 441–451. https://doi.org/10.1016/j.ymssp.2012.01.027.

643 [8] A. Barrias, G. Rodriguez, J.R. Casas, S. Villalba, Application of distributed optical fiber
644 sensors for the health monitoring of two real structures in Barcelona, Structure and
645 Infrastructure Engineering 14 (2018) 967–985.
646 https://doi.org/10.1080/15732479.2018.1438479.
647 [9] M. Allain, O. Ple, N. Prime, E. Roux, P. Vacher, In situ DIC method to determine stress
648 state in reinforced concrete structures, Measurement (Lond) 210 (2023).
649 https://doi.org/10.1016/j.measurement.2023.112483.
650 [10] J. Chakraborty, A. Katunin, P. Klikowicz, M. Salamak, Early crack detection of
651 reinforced concrete structure using embedded sensors, Sensors (Switzerland) 19 (2019).
652 https://doi.org/10.3390/s19183879.
653 [11] P. Prasanna, K.J. Dana, N. Gucunski, B.B. Basily, H.M. La, R.S. Lim, H. Parvardeh,
654 Automated Crack Detection on Concrete Bridges, IEEE Transactions on Automation
655 Science and Engineering 13 (2016) 591–599.
656 https://doi.org/10.1109/TASE.2014.2354314.
657 [12] T. Yamaguchi, S. Nakamura, R. Saegusa, S. Hashimoto, Image-based crack detection
658 for real concrete surfaces, IEEJ Transactions on Electrical and Electronic Engineering 3
659 (2008) 128–135. https://doi.org/10.1002/tee.20244.
660 [13] G. Rodriguez, J.R. Casas, S. Villalba, Shear crack pattern identification in concrete
661 elements via distributed optical fibre grid., Structure and Infrastructure Engineering 15
662 (2019) 1630–1648.
663 [14] I. Fernandez, C.G. Berrocal, R. Rempling, Two-dimensional strain field analysis of
664 reinforced concrete D-regions based on distributed optical fibre sensors, Eng Struct 278
665 (2023). https://doi.org/10.1016/j.engstruct.2022.115562.
666 [15] M.F. Bado, J.R. Casas, A review of recent distributed optical fiber sensors applications
667 for civil engineering structural health monitoring, Sensors 21 (2021) 1–83.
668 https://doi.org/10.3390/s21051818.
669 [16] K. Zdanowicz, D. Gebauer, M. Koschemann, K. Speck, O. Steinbock, B. Beckmann, S.
670 Marx, Distributed fiber optic sensors for measuring strains of concrete, steel, and textile
671 reinforcement: Possible fields of application, Structural Concrete 23 (2022) 3367–3382.
672 https://doi.org/10.1002/suco.202100689.
673 [17] T. Janiak, H. Becks, B. Camps, M. Classen, J. Hegger, Evaluation of distributed fibre
674 optic sensors in structural concrete, Materials and Structures/Materiaux et Constructions
675 56 (2023). https://doi.org/10.1617/s11527-023-02222-9.

[18] C. Zhu, H. Zheng, L. Ma, Z. Yao, B. Liu, J. Huang, Y. Rao, Advances in Fiber-Optic Extrinsic Fabry-Perot Interferometric Physical and Mechanical Sensors: A Review, IEEE Sens J 23 (2023) 6406–6426. https://doi.org/10.1109/JSEN.2023.3244820.

[19] F.I.H. Sakiyama, F. Lehmann, H. Garrecht, Structural health monitoring of concrete structures using fibre-optic-based sensors: A review, Magazine of Concrete Research 73 (2021) 174–194. https://doi.org/10.1680/jmacr.19.00185.

[20] P.K.S. Manish Mishra, Fiber Bragg Gratings in Healthcare Applications: A Review. IETE Technical Review, IETE Technical Review 40 (2023).

[21] J.K. Sahota, N. Gupta, D. Dhawan, Fiber Bragg grating sensors for monitoring of physical parameters: a comprehensive review, Optical Engineering 59 (2020) 1. https://doi.org/10.1117/1.oe.59.6.060901.

[22] H.Y. Qin, Q.X. Shen, W.X. Zhu, H.L. Zhang, Range-expansion technology and fatigue performance study on the self-sensing steel strand with an embedded fibre Bragg grating sensor, Strain 56 (2020). https://doi.org/10.1111/str.12354.

[23] C.Y. Wei, S.W. James, C.C. Ye, R.P. Tatam, P.E. Irving, Application issues using fibre Bragg gratings as strain sensors in fibre composites, Strain 36 (2000) 143–150. https://doi.org/10.1111/j.1475-1305.2000.tb01190.x.

[24] B. Torres Górriz, P. Rinaudo, P.A. Calderón García, Comparison between point and long-gage FBG-based strain sensors during a railway bridge load test, Strain 53 (2017). https://doi.org/10.1111/str.12230.

[25] J. Waldbjørn, J. Høgh, J. Wittrup-Schmidt, M.W. Nielsen, K. Branner, H. Stang, C. Berggreen, Strain and displacement controls by fibre bragg grating and digital image correlation, Strain 50 (2014) 262–273. https://doi.org/10.1111/str.12089.

[26] S. Liu, F. Yu, R. Hong, W. Xu, L. Shao, F. Wang, Advances in phase-sensitive optical time-domain reflectometry, Opto-Electronic Advances 5 (2022). https://doi.org/10.29026/oea.2022.200078.

[27] S.Z. et al. Qinlin Cai, Optical frequency domain reflectometry sensing for damage detection in long-span bridges using influence surface, Struct Health Monit 22 (2023).

[28] P. Lu, N. Lalam, M. Badar, B. Liu, B.T. Chorpening, M.P. Buric, P.R. Ohodnicki, Distributed optical fiber sensing: Review and perspective, Appl Phys Rev 6 (2019). https://doi.org/10.1063/1.5113955.

[29] M. Elsherif, A.E. Salih, M.G. Muñoz, F. Alam, B. AlQattan, D.S. Antonysamy, M.F. Zaki, A.K. Yetisen, S. Park, T.D. Wilkinson, H. Butt, Optical Fiber Sensors: Working

709 Principle, Applications, and Limitations, Adv Photonics Res 3 (2022).
710 https://doi.org/10.1002/adpr.202100371.
711 [30] C., C.D., D.E., M.J., M.C., P.-C.J. Brochier, Système de détection apte à générer un
712 signal électrique représentatif d'une variation d'intensité lumineuse et capteur de
713 pression intégrant un tel système de détection, 2017.
714 [31] ams OSRAM, AS7261 XYZ Chromatic White Color Sensor + NIR with Electronic
715 Shutter and Smart Interface, (2016).
716 [32] M. Richaud, C. Brochier, M. Allain, F. Pellier, D. Briand, N. Briand, O. Plé, Y. De Souza
717 Gomes, M. Saidi, A. Lushnikova, Détecteur de déformation à base de fibres optiques, et
718 procédé de calibration d'un tel détecteur, B256-B-69739, 2024.
719 [33] G.L. Golewski, The Phenomenon of Cracking in Cement Concretes and Reinforced
720 Concrete Structures: The Mechanism of Cracks Formation, Causes of Their Initiation,
721 Types and Places of Occurrence, and Methods of Detection—A Review, Buildings 13
722 (2023). https://doi.org/10.3390/buildings13030765.
723 [34] G. Tiberti, F. Minelli, G.A. Plizzari, F.J. Vecchio, Influence of concrete strength on crack
724 development in SFRC members, Cem Concr Compos 45 (2014) 176–185.
725 https://doi.org/10.1016/j.cemconcomp.2013.10.004.
726 [35] H. Zheng, W. Zhang, B. Li, J. Zhu, C. Wang, G. Song, G. Wu, X. Yang, Y. Huang, L.
727 Ma, Recent advances of interphases in carbon fiber-reinforced polymer composites: A
728 review, Compos B Eng 233 (2022). https://doi.org/10.1016/j.compositesb.2022.109639.
729 [36] G. Paolo Cimellaro, M. Domaneschi, A. Cardoni, D. Inaudi, I. Cottone, F. Ansari, Crack
730 Detection Using Embedded Fiber-Optic Sensors in Reinforced Concrete Beams, n.d.
731 [37] M. Gkantou, M. Muradov, G.S. Kamaris, K. Hashim, W. Atherton, P. Kot, Novel
732 electromagnetic sensors embedded in reinforced concrete beams for crack detection,
733 Sensors (Switzerland) 19 (2019). https://doi.org/10.3390/s19235175.
734 [38] S. Hedan, V. Valle, P. Cosenza, Subpixel precision of crack lip movements by
735 Heaviside-based digital image correlation for a mixed-mode fracture, Strain 56 (2020).
736 https://doi.org/10.1111/str.12346.
737 [39] A. Blug, F. Conrad, A. Bertz, C. Kontermann, D. Carl, M. Oechsner, Application of
738 high-performance DIC for a comprehensive evaluation of biaxial fatigue crack growth
739 experiments, Strain 59 (2023). https://doi.org/10.1111/str.12455.
740 [40] M. Saidi, A. Gabor, Adaptation of the strain measurement in textile reinforced
741 cementitious matrix composites by distributed optical fibre and 2D digital image
742 correlation, Strain 56 (2020). https://doi.org/10.1111/str.12335.

743 [41] A. Armonico, M. Saidi, L. Michel, S. Bel, E. Ferrier, Inverse analysis based on DFOS
744 technology for the study of the bonding behaviour of FRP to concrete beams, Mater
745 Today Commun 35 (2023). https://doi.org/10.1016/j.mtcomm.2023.105655.
746 [42] T.H. Becker, Extracting fracture properties from digital image and volume correlation
747 displacement data: A review, Strain (2023). https://doi.org/10.1111/str.12469.
748 [43] N. Gehri, J. Mata-Falcón, W. Kaufmann, Automated crack detection and measurement
749 based on digital image correlation, Constr Build Mater 256 (2020).
750 https://doi.org/10.1016/j.conbuildmat.2020.119383.
751 [44] J.E.M.C. and I.M.A. (Eds.) International Digital Image Correlation Society, A Good
752 Practices Guide for Digital Image Correlation, (2018).
753 [45] Gom correlate, 3D displacements and strains in motion pictures, (2018).
754 https://www.gom.com/en/products/metrology-software/gom-correlate-pro (accessed
755 January 15, 2024).
756 [46] M.A. Abed, J. Fořt, A. Naoulo, A. Essa, Influence of polypropylene and steel fibers on
757 the performance and crack repair of self-compacting concrete, Materials 14 (2021).
758 https://doi.org/10.3390/ma14195506.
759 [47] C. Chen, Y. Yang, Y. Zhou, C. Xue, X. Chen, H. Wu, L. Sui, X. Li, Comparative analysis
760 of natural fiber reinforced polymer and carbon fiber reinforced polymer in strengthening
761 of reinforced concrete beams, J Clean Prod 263 (2020).
762 https://doi.org/10.1016/j.jclepro.2020.121572.
763 [48] J. Luo, Y. Wang, S. Asamoto, K. Nagai, Mesoscopic simulation of crack propagation
764 and bond behavior in ASR damaged concrete with internal/external restraint by 3D
765 RBSM, Cem Concr Compos 129 (2022).
766 https://doi.org/10.1016/j.cemconcomp.2022.104488.
767 [49] P.M. Ferreira, M.A. Machado, M.S. Carvalho, C. Vidal, Embedded Sensors for
768 Structural Health Monitoring: Methodologies and Applications Review, Sensors 22
769 (2022). https://doi.org/10.3390/s22218320.
770